THE ASTROPHYSICAL JOURNAL, 555:950–960, 2001 July 10

A SUBMILLIMETER STUDY OF THE STAR-FORMING REGION NGC 7129

ANDREEA S. FONT[1] AND GEORGE F. MITCHELL
Department of Astronomy and Physics, Saint Mary's University, Halifax, NS B3H 3C3, Canada
AND
GÖRAN SANDELL[2]
Universities Space Research Association, NASA Ames Research Center, MS 144-2, Moffett Field, CA 94035
Received 2000 July 21; accepted 2001 March 16

ABSTRACT

New molecular (^{13}CO $J = 3$–2) and dust continuum (450 and 850 μm) maps of the NGC 7129 star-forming region are presented. The maps include the Herbig Ae/Be star LkHα 234, the far-infrared source NGC 7129 FIRS 2, and several other prestellar sources embedded within the molecular ridge. The data are complemented with C^{18}O $J = 3$–2 spectra at several positions within the mapped region. Both the submillimeter and the ^{13}CO emission show a similar morphology, displaying a sharp boundary toward the cavity. The submillimeter maps also reveal a second source, SMM 2, which is not clearly seen in any earlier data set. This is either a prestellar core or possibly a protostar. Also, the highest continuum peak emission is identified with the deeply embedded source IRS 6 a few arcseconds away from LkHα 234. These new 450 and 850 μm observations are combined with previous continuum observations of the three compact far-infrared sources in the field, in order to make fits to the spectral energy distributions and to obtain the source sizes, dust temperatures, luminosities, and masses. For nine positions where both ^{13}CO and C^{18}O spectra are available, gas masses have been obtained and compared with masses derived from the continuum fluxes. The masses are found to be consistent, implying little or no CO depletion onto grains. The dust emissivity index is found to be low toward the dense compact sources, $\beta \sim 1$–1.6, and high, $\beta \sim 2.0$, in the surrounding cloud.

Subject headings: dust, extinction — ISM: molecules — stars: formation — stars: individual (LkHα 234) — stars: pre–main-sequence — submillimeter

1. INTRODUCTION

NGC 7129 is a reflection nebula seen against a molecular cloud and estimated by Shevchenko et al. (1989) to be at a distance of 1.25 kpc. There are many signs in this region which support the idea of triggered and possibly ongoing star formation: the association of a very young cluster formed by the B3-type stars BD +65°1637 and BD +65°1638, and the B5/7-type star LkHα 234, several embedded infrared sources (Harvey, Wilking, & Joy 1984; Weintraub, Kastner, & Mahesh 1994; Cabrit et al. 1997), as well as reflection nebulae and Herbig-Haro (HH) objects (Hartigan & Lada 1985; Miranda et al. 1994). There are also several molecular outflows in the region: one associated with an optical jet near LkHα 234 (Ray et al. 1990; Edwards & Snell 1983), another bipolar outflow near the far-infrared source NGC 7129 FIRS 2, and one possibly driven by the T Tauri star V350 Cep (Hartigan & Lada 1985; Goodrich 1986; Miranda et al. 1994).

A molecular cavity is revealed in both molecular and infrared maps (Bechis et al. 1978; Bertout 1987), but its origin is still unknown. The location of the two bright stars, BD +65°1637 and BD +65°1638, inside the cavity suggests three mechanisms by which the molecular cavity could have been created: (1) through the advancement of a photon-dominated region (PDR) around those stars, in which the molecular gas was dissociated by their intense UV radiation; (2) by an expanding shell associated with stellar mass loss; or (3) by radiation pressure acting on grains, together with gas-grain drag (Bechis et al. 1978). The two mid-B–type stars in the cavity, BD +65°1637 and BD +65°1638, are also the oldest in the cluster. Therefore stellar mass loss may have been very effective at earlier times, and the winds from those two stars may have triggered the formation of other bright stars in NGC 7129, including LkHα 234 and SVS 13. As for what mechanism is dominating at present time, the question remains open. PDR models can marginally explain the line fluxes of [O I] and [C II] emission in the region, although the C-type shock models cannot be ruled out (Lorenzetti et al. 1999; Giannini et al. 1999).

This paper employs new, high-resolution submillimeter observations of the molecular ridge in dust continuum emission, ^{13}CO line emission, and C^{18}O line emission. One goal of this study is to improve the present picture of the structure of the ridge and the ridge-cavity boundary. Another goal is to obtain the physical properties of the compact far-infrared sources in the ridge. A third aim is to obtain the gas/dust ratio, thus determining whether CO isotopomers are a good surrogate for molecular hydrogen or whether CO has substantially frozen out onto dust grains. The final goal is to search for variations in the dust opacity with position through the field. The mapped region includes the dense molecular cloud, a photodissociation region, and a powerful outflow. We might expect processes such as grain coagulation and mantle evaporation to have a strong spatial dependency here and for this to be reflected in spatial variations of the dust emissivity index, β.

2. OBSERVATIONS AND DATA REDUCTION

2.1. ^{13}CO *and* C^{18}O *Observations*

Observations of ^{13}CO and C^{18}O $J = 3$–2 were made with the James Clerk Maxwell Telescope (JCMT) on

[1] Department of Physics and Astronomy, University of Victoria, P.O. Box 3055, Victoria, BC V8W 3P6, Canada; afont@noir.phys.uvic.ca.
[2] gsandell@mail.arc.nasa.gov.

Mauna Kea, Hawaii, in 1994 August and 1997 November, respectively, with the receiver B3i and the Digital Autocorrelation Spectrometer (DAS). The observations were made by position switching, with the reference position 10′ east of LkHα 234, which was determined to be free of significant CO emission. The main-beam efficiency (η_{MB}) was 0.58, and the half-power beamwidth (HPBW) was ∼14″ for both ^{13}CO and C^{18}O observations.

A grid map with the spacing of 7.″5 × 7.″5 was taken in the ^{13}CO $J = 3$–2 (330.58 GHz) rotational transition. The map was centered near the star LkHα 234,[3] at coordinates $\alpha(J2000) = 21^h43^m06^s.08$, $\delta(J2000) = 66°06'56''.29$ and extending from −100″ to +100″ in α and from −150″ to 75″ in δ offsets. The instrumental velocity resolution was 0.28 km s^{-1}. C^{18}O $J = 3$–2 (329.33 GHz) spectra were taken at nine positions around the star LkHα 234 and near the molecular ridge. Figure 1 shows the ^{13}CO integrated intensity ($\int T_B\, dv$) contour map superposed on a K' image of the NGC 7129 region from Hodapp (1994). The nine C^{18}O offsets with respect to the star LkHα 234 are shown with crosses.

[3] The astrometric position for LkHα 234 given by Clements & Argyle (1984) is $\alpha(J2000) = 21^h43^m06^s.802$, $\delta(J2000) = 66°06'54''.5$.

2.2. *Submillimeter Continuum Observations*

Two deep 850 and 450 μm maps of LkHα 234 and the bright-rimmed cloud ridge southwest of LkHα 234 have been obtained using the Submillimeter Common User Bolometer Array (SCUBA; Holland et al. 1999) on the 15 m JCMT on 1997 October 15. The weather conditions were dry and stable with an 850 μm zenith optical depth of ∼0.19. The two overlapping fields were obtained in jiggle-map mode with a chop-throw of 150″ in R.A. with a total integration time of 85 minutes field^{-1}. For a description of SCUBA and its observing modes, see Holland et al. (1999). Unfortunately, the maps were taken without usable calibration and pointing observations, and we have therefore reduced the data by determining the HPBW of the telescope from observations of Uranus from other nights in September and October with similar sky conditions. The same nights were also used to determine gain conversion factors for the 850 and 450 μm filters. The HPBW was found to be ∼15.″6 × 13.″5 at 850 μm and 9.″1 × 7.″8 at 450 μm with the beam broadened in the chop direction. The submillimeter position of LkHα 234 (Table 3), which has an accuracy of ∼1″, was taken from three short-integration maps interlaced with pointing observations in SCUBA commissioning time during spring 1997. These maps have not been added

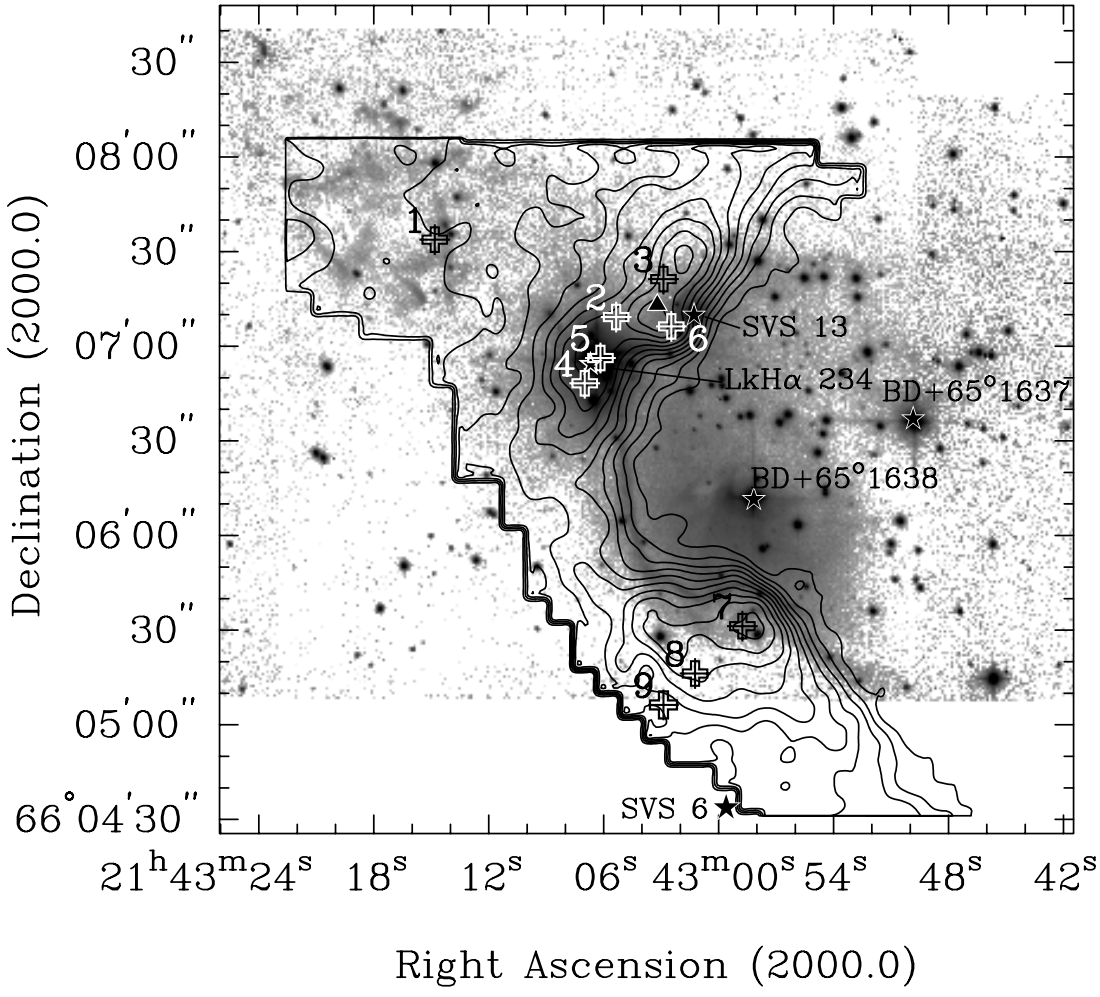

FIG. 1.—^{13}CO $J = 3$–2 integrated intensity map superposed on a K' image of the region (Hodapp 1994). The map was centered near the star LkHα 234, with the center coordinates $\alpha(J2000) = 21^h43^m06^s.08$, $\delta(J2000) = 66°06'56''.29$, and extending from −100″ to +100″ in α offsets and from −150″ to 75″ in δ offsets. The crosses indicate the nine offsets with complementary C^{18}O $J = 3$–2 data which have been chosen for analysis (the numbers correspond to Table 2 entries).

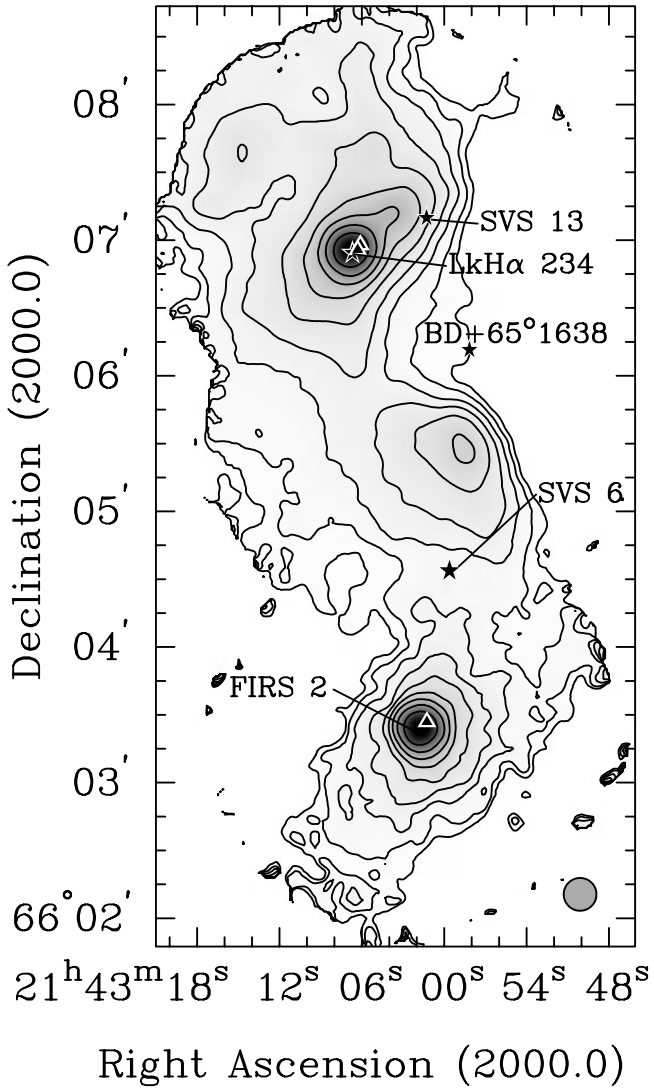

FIG. 2.—Composite 850 μm map of LkHα 234 and NGC 7129 FIRS 2 in gray scale overlaid with contours. The 850 μm flux density is contoured from 50 mJy beam^{-1} in logarithmic steps equal to a factor of $10^{0.2}$ of the previous level. The size of the beam, 14".5, is indicated at the bottom right of the plot. Near-IR sources are labeled by stars and H_2O masers by triangles.

in the final data set, because they were taken with a 120" azimuth chop, and there is clear evidence that the array was chopping onto emission. However, if we compare the total flux density of LkHα 234 (i.e., background subtracted flux density), it agrees very well with data taken in October.

We also include a map of the H_2O maser and bipolar outflow source NGC 7129 FIRS2, which was used as a test source during SCUBA commissioning time (Sandell 1997). A composite map at 850 μm, including all the three overlapping fields, is shown in Figure 2.

The basic data reduction was done with SURF (Jenness & Lightfoot 1999). Even with a 150" chop, it is more than likely that we may have chopped onto some emission in both fields, but it does not appear to affect the morphology of the strong dust ridge in which LkHα 234 is embedded. Some negative emission is detected west of LkHα 234, which confirms that there is some emission in the off-position. It is therefore likely that emission east of the ridge is also affected, which is why the 850 and 450 μm maps appear somewhat different. To map a cloud ridge in beam switch mode is not very advisable, but at the time SCUBA was available only in jiggle map mode. Although chopping into the cloud cannot be avoided, as long as the off-source emission is faint and relatively uniform, the morphology of the cloud ridge should not be affected. However, since the beam size and error lobe contribution differ between 850 and 450 μm, this leads to systematic errors in the integrated intensities (§ 3.2).

The peak fluxes are uncertain to about 10% for 850 μm and 20% for 450 μm. The final pointing corrected and calibrated maps have an rms noise of $\sim$15 mJy beam^{-1} and $\sim$120 mJy beam^{-1} for 850 and 450 μm, respectively. These maps were written out as FITS files and read into the MIRIAD package (Sault, Teuben, & Wright 1995) for further analysis.

3. ANALYSIS

3.1. ^{13}CO *and* C^{18}O *Emission*

A sharply bounded molecular cavity is seen in ^{13}CO $J = 3$–2 emission westward of LkHα 234, most probably excavated by the B3-type star BD +65°1637. The lack of molecular emission and the ridge morphology were also noted in the CO $J = 1$–0 and NH_3 observations (Bechis et al. 1978; Fuente et al. 1998; Güsten & Marcaide 1986). However, our high-resolution (half-beam sampling with a 14" beam size) observations resolve the ridge structure in much more detail.

There are four ^{13}CO peaks along the ridge, visible in Figure 1 as contour peaks. These ^{13}CO structures are assumed to be physical clumps and named NGC 7129 CO1, NGC 7129 CO2, NGC 7129 CO3, and NGC 7129 CO4. The positions of these four ^{13}CO peaks, together with their peak antenna temperatures, line widths, and line center velocities for the ^{13}CO emission, are given in Table 1. NGC 7129 CO1 coincides within errors with LkHα 234 (position

TABLE 1

PHYSICAL PARAMETERS OF THE ^{13}CO PEAKS

Source	α(J2000)	δ(J2000)	T_A^* (K)	Δv (km s^{-1})	v_{center} (km s^{-1})
NGC 7129 CO1.....	21 43 06.7	+66 06 57.0	13.08	2.96	−10.30
NGC 7129 CO2.....	21 43 03.5	+66 07 10.0	15.02	1.21	−10.16
NGC 7129 CO3.....	21 43 02.0	+66 07 28.0	15.89	1.24	−10.12
NGC 7129 CO4.....	21 42 58.5	+66 05 30.0	17.55	1.44	−10.39

NOTE.—Units of right ascension are hours, minutes, and seconds, and units of declination are degrees, arcminutes, and arcseconds. The peak antenna temperature, the line width, and line velocity center were determined with a Gaussian model best fit of the spectral lines.

TABLE 2

MEASURED PROPERTIES OF THE GAS FOR THE NINE OFFSETS WHERE BOTH $C^{18}O$ AND ^{13}CO OBSERVATIONS ARE AVAILABLE

Number	Offset (arcsec)	$T_A^*(^{13}CO)$ (K)	T_A^* ($C^{18}O$) (K)	τ_{13}	T_{ex} (K)	M_{gas} ($M_\odot$/14″ beam)
1	(52.5, 37.5)	3.84	1.32	4.13	13.1	3.6
2	(−5.0, 13.0)	12.57	4.43	4.27	29.2	7.3
3	(−20.0, 25.0)	15.73	7.68	6.69	34.7	12.8
4	(5.0, −8.0)	13.13	3.87	3.35	30.7	11
5	(0.0, 0.0)	12.8	4.18	3.85	29.8	10.7
6	(−22.5, 10.0)	14.97	4.96	3.92	33.6	7.2
7	(−45.0, −85.0)	17.54	5.70	3.82	38.3	8.3
8	(−30.0, −100.0)	13.04	3.25	2.63	31.5	6.7
9	(−20.0, −110.0)	7.84	2.97	4.71	20.6	6.4

NOTE.—The last two columns in the table were calculated assuming LTE conditions and that the gas is thermalized.

5 in Table 2) and NGC 7129 CO4 with position 7; the other two clumps, NGC 7129 CO2 and NGC 7129 CO3, are located close to the positions 6 and 3, respectively.

Perhaps the most striking feature of the ^{13}CO map is the sharpness of the transition between the molecular cavity to the west and the molecular cloud to the east. ^{13}CO line strengths drop by factors of 20 or more across the boundary. The narrowness of the transition region between atomic and molecular gas has implications for the three-dimensional topology of the region. There seem to be three possibilities: First, the boundary region may be a sheet which happens to be perpendicular to the line of sight. Second, the molecular cavity may be a bowl, which is surrounded by molecular gas. Third, the molecular cloud may take the form of a rather narrow ridge, which is partially surrounded by atomic gas. The first possibility is improbable, while the second should lead to a broader transition region (molecular to atomic). We favor the third picture, in which the dense portion of the molecular cloud consists of a clumpy ridge with a line-of-sight extent comparable to its extent in the plane of the sky (roughly 0.5 pc).

Another remarkable feature which can be seen in Figure 1 is the narrow filament of emission seen in the K' image (Hodapp 1994). It extends roughly south from LkHα 234 and then curves to the west, keeping a nearly constant surface brightness. In an unpublished observation using an IR camera with a circularly variable filter on the Canada-France-Hawaii Telescope, G. F. Mitchell and D. Nadeau found this filament to be also a source of strong emission in the $S(1)$ $v = 1$–0 line of H_2. The optical filament follows closely the outermost ^{13}CO contours, which separate the cavity from the molecular cloud. Can this close vicinity be explained by standard PDR models? The presence of the photodissociation region is a natural explanation for both the sharp molecular boundary and the line-emitting filament. The H_2 $S(1)$ $v = 1$–0 line emission is then due to fluorescence. The PDR is very likely produced by UV radiation from the early B star BD +65°1638. However, the detection of all three types of emission optical, CO and H_2 $v = 1$–0, at the same location is in contrast with predictions of steady state stationary PDR models (Hollenbach & Tielens 1997). These models predict a more gradual succession of emission layers as one moves away from the UV ionization front and where the H_2 $v = 1$–0 transition layer would be separated by about 10″ from the molecular CO emission. On the other hand, the observed morphology may be explained in the framework of nonstationary PDR models (Bertoldi & Draine 1996), which show that the inhomogeneities in the molecular cloud surface can lead to the merging of the ionization and the dissociation front.

TABLE 3

POSITIONS AND DECONVOLVED GAUSSIAN SIZES OF COMPACT SUBMILLIMETER SOURCES

Source	α(J2000.0)	δ(J2000.0)	$\theta_a \times \theta_b$ (arcsec)	P.A. (deg)
LkHα 234 SMM 1	21 43 06.76	+66 06 56.0	6.1 × 4.9	−46
LkHα 234 SMM 2	21 43 03.20	+66 07 13.1	14.6 × 9.6	−67
NGC 7129 FIRS 2.....	21 43 01.51	+66 03 24.2	3.9 × 3.7	...

NOTE.—Units of right ascension are hours, minutes, and seconds, and units of declination are degrees, arcminutes, and arcseconds.

Because ^{13}CO is likely to have an appreciable optical depth, $C^{18}O$ $J = 3$–2 spectra were obtained at several positions. The positions for which we have $C^{18}O$ spectra are marked by the cross symbols in Figure 1. A comparison between the ^{13}CO and $C^{18}O$ spectra at the nine offset positions is shown in Figure 3. Positions are given as offsets in arcseconds from LkHα 234. The line intensities are given in antenna temperatures, T_A^*, after corrections for losses due to Earth's atmosphere and the telescope. For all spectra, only the linear baselines were removed, using the SPECX software package (Padman 1992).

Near LkHα 234, the lines are broadened due to contributions from the outflow. Position 1 (Table 2) is near the peak of CO emission in the redshifted outflow lobe. Both the ^{13}CO and $C^{18}O$ spectra are double peaked at this position. The value of the line ratio shows that $C^{18}O$ is optically thin. The two peaks therefore represent two real kinematic components rather than a single line suffering self-absorption. The peak at -10 km s^{-1} is the ambient gas at this position, while the peak at -7 km s^{-1} is the postshock gas.

Several line parameters have been calculated at each offset, assuming local thermodynamical equilibrium (LTE) conditions. A value of 10 was used for the abundance ratio $N_{^{13}CO}/N_{C^{18}O}$, estimated from the partial ratios $N_{C^{18}O}/N_{H_2} \sim 2 \times 10^{-7}$ (Frerking, Langer, & Wilson 1982) and the standard value $N_{^{12}CO}/N_{^{13}CO} \sim 56$ (Wilson & Rood 1994). The intensity ratio, $^{13}CO/C^{18}O$, was used to find the optical depth, assuming a common T_{ex} for the two transitions. The value of T_{ex} was computed from the LTE expression relating line strength (given by the radiation

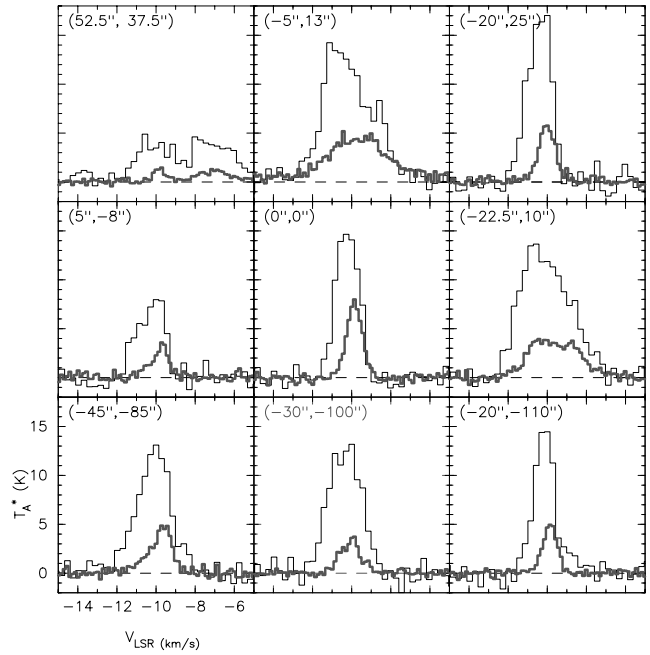

FIG. 3.—^{13}CO and C^{18}O $J = 3$–2 spectral lines shown superposed for the nine offsets marked in Fig. 1 and listed in Table 2. The thin lines correspond to ^{13}CO emission and the thick lines to C^{18}O emission.

temperature), line optical depth τ, and the excitation and radiation temperatures:

$$T_{ex} = \frac{h\nu}{k} \frac{1}{\ln[1 + (1 - e^{-\tau})h\nu/kT_R]} . \quad (1)$$

In the above relation, the radiation temperature, T_R, is related to the antenna temperature, T_A^*, by

$$T_R = \frac{T_A^*}{\eta_{MB} f} , \quad (2)$$

where the beam efficiency η_{MB} was 0.58 and the filling factor f was assumed to be 1. We will further assume that the gas kinetic temperature is equal to the excitation temperature but caution that a density greater than 10^4 cm^{-3} is required for this to be true. The results of the LTE analysis are shown in Table 2. For LkHα 234, the excitation temperature is found to be about 30 K, in agreement with previous values of 20–30 K obtained from lower resolution (70″) CO observations (Bechis et al. 1978) and with the 20–25 K obtained from NH_3 (40″) observations (Güsten & Marcaide 1986).

At position 6 (Table 2), the gas has an excitation temperature of $\sim$34 K, which is higher than the typical value for a dark core but lower than the previous value of 63 K obtained by Mitchell & Matthews (1994) from ^{12}CO and ^{13}CO data. These two temperatures can be reconciled, taking into account that the isotopomers from which they have been derived (^{12}CO for 63 K and ^{13}CO for 34 K) have different optical depths and hence probe different regions of the gas. With its lower optical depth, ^{13}CO will probe deeper into the PDR, where the temperature is lower.

The three last entries in Table 2 represent positions increasing in distance from the cloud boundary. The excitation temperature is found to decrease with distance from the boundary, from 38 K through 31 K to 21 K. This decrease is expected as the stellar radiation is increasingly attenuated with distance into the molecular cloud. At position 1 (Table 2), which is farthest from the cloud boundary, the excitation temperature of the ambient gas is lowest, $\sim$13 K.

Since the clumps have approximately the same size as our beam and since the beam does not always include a clump of gas, it is reasonable to calculate the masses of the gas within the beam (14″). The results, including the fractional He abundance and assuming a distance of 1.25 kpc to the source, are shown in Table 2. The NGC 7129 CO1 clump which coincides with LkHα 234 contains 10.7 $M_\odot$. The masses within the beam, at the two offsets adjacent to the clump matching the prestellar source LkHα 234 SMM 2 (positions 3 and 6 in Table 2), are 12.8 and 7.2 $M_\odot$, respectively. However, those values should be regarded as upper limits since the temperatures are probably lower, as suggested by the more optically thin NH_3 data.

These results also depend on the accuracy in the distance determination. The distance estimate of 1 kpc to NGC 7129, reported by Racine (1968), has been most commonly used. In our analysis we have adopted the value of 1.25 kpc, determined by Shevchenko et al. (1989) from an improved photometry and spectral classification of 35 stars. However, if the PDR is associated with to the Cepheus Bubble, as suggested by Ábrahám, Balázs, & Kun (2000), then the distance to could be as low as 500–700 pc, and of course the derived masses and luminosities would be significantly reduced.

The masses obtained in this analysis will be discussed and compared to masses obtained from the dust emission, in § 4 below.

3.2. *Dust Emission*

In order to compare the 850 and 450 μm dust emission with the molecular line observations, the 450 μm images need to be convolved to the same HPBW as the rest of the observations. However, since the JCMT is far from perfect at 450 μm, one first needs to remove the error beam. A model beam was therefore constructed, by fitting three Gaussians to representative beam maps of Uranus. The main beam and the near error lobe were fitted with elliptical Gaussians, while the far error lobe was fitted with a circularly symmetric beam. The relative amplitude of the main beam and the near and far error lobes were found to be 0.925:0.07:0.005. The HPBW of the near error lobe was 37″ × 26″, with the major axis aligned in the chop direction similarly to the main beam (see § 2.2), and the far error lobe gave a HPBW $\sim$ 120″. The deconvolution of images was tested with both MAXEN (MIRIAD's maximum entropy task) and CLEAN. Both worked reasonably well, but CLEAN is better in preserving flux and was therefore adopted. We also constructed a model beam for 850 μm and ran CLEAN on the 850 μm images as well. The deconvolved images were restored with a symmetric Gaussian to a 14″ beam. For 450 μm we also made maps restored to a HPBW of 8″. Figure 4 shows the high-resolution maps at 450 and 850 μm.

Even CLEAN, however, is not ideal for recovering smooth extended emission, which could cause us to underestimate the 450 μm emission more than at 850 μm, since the 450 μm map is restored from an 8.″5 resolution to 14″, while the resolution in the 850 μm maps remains roughly the same. Emission in the off position will have an even more severe systematic effect. Since the error beam has a much higher amplitude at 450 μm than at 850 μm, any

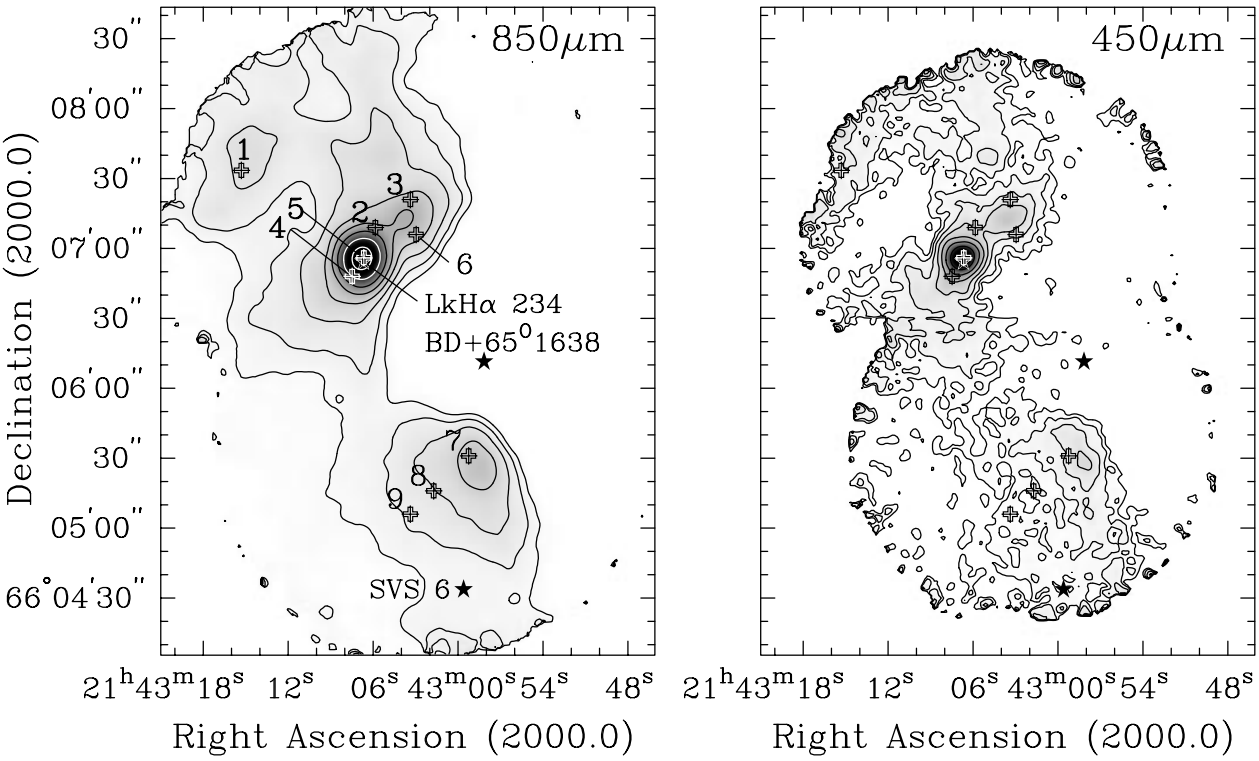

FIG. 4.—Contour maps of deconvolved images at 850 μm (14″ beam) and 450 μm (8″ beam). For 850 μm the contour levels start from 100 mJy beam^{-1} and go in steps equal to a factor of $10^{0.2}$ of the previous level. For 450 μm the contour levels start at 250 mJy beam^{-1} and go in steps of $10^{0.25}$ of the previous level.

emission in the off position will affect the base level of the 450 μm map much more than that at 850 μm. This leads to a systematic underestimate of the flux densities at 450 μm. This was tested by adding a constant flux level of 5% of the peak value at 450 μm to the "raw" 450 μm map of LkHα 234. The base level corrected map was run through CLEAN and restored to 14″. When the flux densities in the 14″ beam are compared for positions more than 40″ away from LkHα 234, it is found that adding a zero level of 5% of the peak flux density increases the flux level by more than a factor of 2 compared to the uncorrected map. Since the base level can easily have an error of 5%, this means that the flux densities for faint extended emission are uncertain by more than a factor of 2. In this case the 450 μm flux densities are more than likely to be systematically underestimated.

Two-dimensional Gaussian fits were then used to determine the size and total flux of the two "compact" sources in the field, i.e., LkHα 234 SMM 1 and the protostellar source LkHα 234 SMM 2, $\sim$28″ northwest of LkHα 234 SMM 1. Here the flux estimates are much more accurate since the sources are compact and the emission from the surrounding cloud ridge can be subtracted. LkHα 234 SMM 1 emission is found to be extended, with a size of $\sim$5″ (Table 3). This agrees well with earlier 800 and 450 μm maps (Sandell & Weintraub 1994) as well as with 1.3 mm maps by Fuente et al. (1998) and Henning et al. (1998). The source LkHα 234 SMM 2 is not obvious in the 1.3 mm data of Fuente et al. (1998) nor in the map published by Henning et al. (1998), but both 1.3 mm maps show an extension toward SMM 2 in good agreement with our SCUBA maps. By using the size derived from our SCUBA maps, we derive an integrated 1.3 mm flux of 0.2 $\pm$ 0.04 Jy for the map published by Fuente et al. (1998). We are interested to derive the β index (where β reflects the change in dust emissivity or, equivalently, the change in optical depth, with frequency, $\kappa \propto \tau \propto \nu^{\beta}$) and the total (gas + dust) mass. For this, we have fitted the 1.3 mm data point and the two SCUBA data points with a simple isothermal model (see, e.g., Sandell 2000). Since both *IRAS* and Kuiper Airborne Observatory (KAO) data (Bechis et al. 1978; Harvey et al. 1984; Di Francesco, Evans, & Harvey 1998) employ large beam sizes that are likely to include hot dust from the surrounding reflection nebulosity as well, we have not included far-IR data in our least-squares fit, although we constrained our LkHα 234 SMM 1 model to the peak dust temperature derived by Harvey et al. (1984). The results of the fit are given in Table 4 and are

TABLE 4

PHYSICAL PROPERTIES OF THE DECONVOLVED COMPACT SUBMILLIMETER SOURCES

Source	$S_{850\ \mu m}$ (Jy)	$S_{450\ \mu m}$ (Jy)	T_d (K)	β	M_{tot} ($M_\odot$ beam)	L_{dust} ($L_\odot$)
LkHα 234 SMM 1.....	3.12	20.7	45	1.24	7.6	8.8×10^2
LkHα 234 SMM 2.....	0.73	6.2	30	1.62	4.8	1.4×10^2
NGC 7129 FIRS 2.....	3.35	18.1	42	1.04	7.0	4.3×10^2

also shown in Figure 5. LkHα 234 SMM 2 is even less constrained. However, by looking at gas temperatures, either from our own CO observations or at the temperature estimates from the NH_3 map by Güsten & Marcaide (1986), we find the gas temperatures to be ≤ 30 K. Therefore, the fit presented in Table 4 was constrained to 30 K. The mass we derive for the dust disk or envelope surrounding LkHα 234 SMM 1 (Dent et al. 1989) is about half of that derived by Henning et al. (1998) after it is adjusted to the same distance. The difference is largely due to the difference in the adopted mass opacity for the dust.

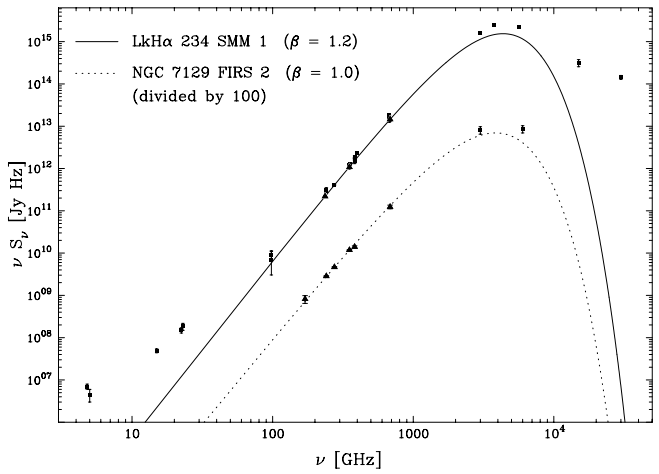

FIG. 5.—Dust fits for LkHα 234 SMM 1 and NGC 7129 FIRS2, the latter data being offset by a factor of 100. The data points include our SCUBA observations, previously unpublished UKT14 data (G. Sandell 2001, private communication), as well as *IRAS* and KAO data (Bechis et al. 1978; Harvey, Wilking, & Joy 1984). The latter observations were not considered in the fit, since they are likely to include hot dust from the surrounding reflection nebulosity, because of their large beam sizes. Fitted data points are marked with filled triangles and all other by filled squares.

In order to compare the gas mass estimates derived from our ^{13}CO and $C^{18}O$ data with dust mass estimates, submillimeter flux densities have been derived from our submillimeter maps convolved with a 14″ beam. The results are given in Table 5. If one uses the baseline unadjusted 450 μm data and ignores the differences in dust properties and dust temperatures between the two embedded stars by assuming that the dust is at the same temperature as the CO, the β-values appear implausibly low. If instead the baseline adjusted 450 μm data were to be used one would obtain a β of ∼1.7. However, since we cannot accurately correct for the emission in the off position, we prefer to assume a β-index and use only the flux density measurements at 850 μm, which are much less affected by emission in the off position. The CO temperatures are likely to be dominated by the gas heated by the PDR, and they therefore give only an upper limit to the mass averaged gas temperatures. The dust emission, however, is more optically thin and the submillimeter dust emission contains also emission from the colder dust inside the dense cloud ridge. This regime is more accurately measured by NH_3, which shows kinetic temperatures of ∼25 K (Güsten & Marcaide 1986) along the cloud ridge. In the second entry for each offset lower gas temperatures are assumed, which are typically smaller than the CO temperatures. The two compact sources in the ridge have been subtracted from the map in order to separate the dust cloud from the disk/envelope emission. However, the total mass values in Table 5 include also the contribution from LkHα 234 SMM 1 and LkHα 234 SMM 2.

3.3. *NGC 7129 FIRS 2*

NGC 7129 FIRS 2 was first discovered by Bechis et al. (1978) as a cold far-IR source associated with a ^{13}CO column density peak south of LkHα 234. It was found to coincide with an H_2O maser (Cesarsky et al. 1978; Rodríguez et al. 1980; Sandell & Olofsson 1981), suggesting

TABLE 5

DUST PROPERTIES FOR THE NINE $C^{18}O$ POSITIONS

Offsets (arcsec)	$S_{850\ \mu m}$ (Jy/14″ beam)	$S_{450\ \mu m}$ (Jy/14″ beam)	T_d (K)	β	M_{tot} ($M_\odot$/14″ beam)
(52.5, 37.5)	0.26	1.39	13.1	1.71	6.5
	0.26		13.1	2.0	9.3
(−5.0, 13.0)	0.74	6.36	29.2	1.70	5.5
	0.43[a]		25.0	2.0	8.2
(−20.0, 25.0).....	0.45	5.18	34.7	2.06	4.1
	0.26[a]		25.0	2.0	4.6
(5.0, −8.0)	1.44	11.6	30.7	1.58	8.6
	0.47[a]		25.0	2.0	8.5
(0.0, 0.0)	3.05	23.1	29.8	1.50	13.9
	0.35[a]		25	2.0	11.2
(−22.5, 10.0).....	0.47	4.15	33.6	1.68	2.8
	0.19[a]		25.0	2.0	4.3
(−45.0, −85.0).....	0.42	3.33	38.3	1.46	1.6
	0.42		25	2.0	5.9
(−30.0, −100.0).....	0.19	2.24	31.5	2.14	2.2
	0.19		25.0	2.0	2.5
(−20.0, −110.0).....	0.13	1.83	20.6	2.67	7.4
	0.13		20.0	2.0	2.3

NOTE.—The second entry for each offset uses the cloud emission only (when applicable) and a value of 2 for the β index.

[a] Cloud emission only; emission from LkHα 234 SMM 1 and LkHα 234 SMM 2 has been subtracted.

that it is a young protostellar source, yet the source is invisible in the optical and near-IR. Additional far-IR mapping by Harvey et al. (1984) confirmed the discovery by Bechis et al. (1978) and detected the source at both 50 and 100 μm, but not at 20 μm or shorter wavelengths. Edwards & Snell (1983) found that FIRS 2 was associated with a CO outflow, which further strengthened its association with a young, intermediate pre–main-sequence star. Jenness, Scott, & Padman (1995) included FIRS 2 in their survey of far-IR cores in the vicinity of H_2O masers and reported a flux density of 5.2 Jy at 800 μm and 30 Jy at 450 μm. Eiróa, Palacios, & Casali (1998) proposed that FIRS 2 is an intermediate-mass class 0 object, based on submillimeter photometry at 2 mm, 1.3 mm, 1.1 mm, and 800 μm, as well as from high-resolution reconstructed IRAS data. They detected FIRS 2 at 25, 60, and 100 μm, but not at 12 μm. They fitted the spectral energy distribution of FIRS 2 with a standard isothermal graybody fit and found a β-index of 0.9 and a dust temperature of 35 K corresponding to a total mass of 6 $M_\odot$.

Our SCUBA data give a more accurate position for FIRS 2 (Table 3), which agrees well with the H_2O position (uncertainty $\pm 10''$). The source is resolved with a FWHM of $\leq 3''.7$. The surrounding cloud core is also seen, but because most observations were made using relatively short chop throws ($\sim 100''$), the emission of the cloud core is not well mapped. The data is supplemented with maps and photometry made by us using UKT14 on JCMT. Our UKT14 flux densities are generally lower than those found by Jenness et al. (1995) and Eiróa et al. (1998) but agree much better with the well-calibrated SCUBA data. We find flux densities of 0.48 ± 0.10, 1.18 ± 0.03, 1.69 ± 0.05, and 3.66 ± 0.22 Jy for 2 mm, 1.3 mm, 1.1 mm, and 800 μm, respectively. The flux densities at 2 and 1.3 mm are based on photometry and therefore also include a small contribution from the surrounding cloud. The 1.1 mm and 800 μm values are derived from Gaussian fits to calibrated maps, i.e., essentially the same way SCUBA data were analyzed.

The isothermal fit (Fig. 5) predicts a $\beta \sim 1$ for dust temperature of 42 K. The fit underestimates slightly the far-IR data points, which are observed with a large beam size and therefore also include emission from the surrounding cloud core. Our β-index and mass (Table 4) agree rather well with the value derived by Eiróa et al. (1998) and demonstrate that FIRS 2 is a cold protostellar source with a luminosity of $\sim 400\ L_\odot$.

4. DISCUSSION

4.1. *A Gas and Dust Comparison*

The ^{13}CO emission (Fig. 1) and dust emission (Fig. 4) show broadly similar distributions. The molecular cavity is also a dust cavity, although the boundary appears broader in dust continuum emission than in ^{13}CO emission. The presence of a dust cavity suggests that the interior is not filled with H I but has been substantially cleared of dust and gas. Bechis et al. (1978) showed that radiation pressure from older stars in the cavity is capable of doing this. Moreover, recent 21 cm H I observations by H. E. Matthews et al. (2001, in preparation) in the NGC 7129 region support this hypothesis, by showing that H I in the cavity has a low number density, 85 cm^{-3}, and that it is in pressure equilibrium with the molecular gas in the ridge (both having $P/k \sim 2 \times 10^5$ cm^{-3} K).

In both ^{13}CO and dust, the mapped region is seen to contain two main clumps, one surrounding the star LkHα 234 and extending to the northwest, the second being about 2′ to the south. Although the dust and gas maps are consistent on large scales, there are significant differences on smaller scale. The southern clump, centered on the peak NGC 7129 CO4, has an extension to the east with no counterpart in the continuum maps. LkHα 234 SMM 1 (identified as NGC 7129 CO1) dominates the emission in submillimeter, while NGC 7129 CO2 (SMM 2 in Table 3) is almost equally bright in ^{13}CO and much fainter in dust continuum. The peak NGC 7129 CO3 is not present in the dust emission maps. The two ^{13}CO peaks, NGC 7129 CO2 and CO3, have essentially equal intensity, so the difference in continuum emission between the two is surprising. The answer may lie in the proximity of the star SVS 13 to SMM 2. Radiation from SVS 13 may be responsible for maintaining the dust temperature of ~ 30 K, which we find for this source. The projected distance of SMM 2 from SVS 13 is about 3 times that of NGC 7129 CO2, and therefore the stellar radiation field is less intense. However, the absence of dust emission at NGC 7129 CO3 cannot be explained by temperature alone. It must have a lower density than NGC 7129 CO2.

A quantitative comparison of gas and dust is provided by the masses listed in Tables 2 and 5. The mass from the CO isotopomers was obtained from LTE expressions (§ 3.1), while the mass from the 850 μm flux required values of β, T_d, and a gas/dust mass ratio of 100 (Hildebrand 1983):

$$M(M_\odot) = 1.88 \times 10^{-2} \times F \times \left(\frac{\lambda}{0.25}\right)^{\beta+3} \times (e^{14.4/\lambda T_d} - 1) \times d^2 , \quad (3)$$

where F is the flux (in Jy) at the wavelength λ (in mm), d is the distance to the source (in kpc), and the mass opacity coefficient is 10 cm^2 g^{-1} at 250 μm. Two values for dust masses are given in Table 5, for different values of T and β. We will refer below to those found with $\beta = 2$, which is the typical value expected from theoretical grain models (Hildebrand 1983). In view of all the assumptions that have been made, we consider the mass values derived from the CO and from the dust to be in good agreement. In the worst cases, the difference is a factor of 3. In all these cases, the agreement could be improved by making defensible adjustments to the dust temperature. The results are also consistent with little or no CO depletion in the NGC 7129 ridge, perhaps due to the enhanced radiation field, which maintains grain temperatures above the 16 K CO freeze-out temperature.

4.2. *The Nature of the Submillimeter Sources LkHa 234 SMM 1 and SMM 2*

Early studies of NGC 7129 (Bechis et al. 1978; Harvey et al. 1984) indicated that the far-IR emission could be explained by dust heated by the B stars that illuminate the reflection nebulae. The far-IR emission peaked on LkHα 234, which was also known to be a weak radio continuum source (Bertout & Thum 1982), associated with an H_2O maser (Cesarsky et al. 1978) and driving a high-velocity CO outflow (Edwards & Snell 1983). The second far-IR peak, FIRS 2, was also associated with an H_2O maser and a high-velocity CO outflow but lacked an optical counterpart (§ 3.3). Since LkHα 234 was associated with HH objects

(Hartigan & Lada 1985), coincided with a free-free emission source at 15 and 22 GHz, with compact dust emission at 3 mm (Wilking, Mundy, & Schwartz 1986), and drove a highly collimated optical jet (Ray et al. 1990), this identification appeared rather secure.

However, Skinner, Brown, & Steward (1993) noticed that the free-free emission was offset by $\sim 1\farcs7$ from the optical position of LkHα 234 if they adopted the more accurate optical position given by Herbig & Bell (1988) or by $2\farcs2$ when compared with the astrometric position of Clements & Argyle (1984). Near-IR polarimetric imaging by Weintraub et al. (1994) showed that there is a deeply embedded companion $\sim 3''$ northwest of LkHα 234, which was invisible in total intensity maps at K band. High-resolution mid-IR imaging by Cabrit et al. (1997) identified the embedded companion star, IRS 6, at $2\farcs7$ northwest of LkHα 234 and showed that it has a steeply rising spectrum, making IRS 6 as bright as LkHα 234 at 17 μm. IRS 6 therefore coincides with the radio free-free emission source, with two H_2O maser spots, and with the 3 mm dust emission (Wilking et al. 1986; G. Sandell, unpublished data). Cabrit et al. (1997) show that IRS 6 illuminates an arc-shaped reflection nebula with very red colors and that it drives an H_2 jet at a position angle (P.A.) of 226°. The P.A. of the H_2 jet differs from that of the optical [S II] jet, which has a P.A. of 252° (Ray et al. 1990). Whether the much larger [S II] jet also originates from IRS 6 is not clear (Cabrit et al. 1997). Although Mitchell & Matthews (1994) report that the P.A. of the CO outflow agrees with the optical jet, this is not true if the P.A. is determined from the symmetry axis of the large-scale red CO outflow, which is ~230°. Neither does the P.A. of the optical jet agree with the location of the two HH objects GGD 32 and HH 103 SW of LkHα 234 and IRS 6, which lie in the blueshifted lobe of the CO outflow.

The submillimeter position for LkHα 234 SMM 1 determined from our 850 μm map (Table 3) falls between LkHα 234 and IRS 6, but since our positional accuracy is $\sim 1''$, the emission could peak on either star. However, since the dust emission at 3 mm peaks on IRS 6, it is plausible to assume that the submillimeter emission also peaks on IRS 6. It therefore appears that it is the cold, heavily obscured IRS 6 that drives the CO outflow and which is associated with the massive dust disk or envelope we see in the submillimeter. This disklike structure is orthogonal to the near-IR H_2 jet to within a few degrees. From our simple isothermal modeling (§ 3.2) we derive a luminosity of $\sim 9 \times 10^2\ L_\odot$, which would make IRS 6 an early B star, i.e., a young Herbig Be star still heavily enshrouded by dust. It is clear that LkHα 234 as well as BD +65°1638 and even BD +65°1637 and SVS 13 contribute to the 50 and 100 μm emission, but the submillimeter emission is totally dominated by IRS 6 and the second submillimeter source LkHα 234 SMM 2. There is some dust emission in the molecular cavity as well, especially in the vicinity of BD+65°1638. This dust is hotter than the dust in the cloud ridge, which is also seen from the spectral index plot (Fig. 6).

The submillimeter source LkHα 234 SMM 2 does not have a known optical or IR counterpart. It is $\sim 12''$ to the east of SVS 13, which does not appear to be associated with any dust emission (Fig. 4). SMM 2 does not coincide with the CO hot spot seen by Mitchell & Matthews (1994) either, which is $\sim 10''$–$15''$ southeast of the submillimeter source. SMM 2 coincides within errors with the NGC 7129 CO2 peak (Fig. 1) and is also apparent in the CS $J = 3$–2 map

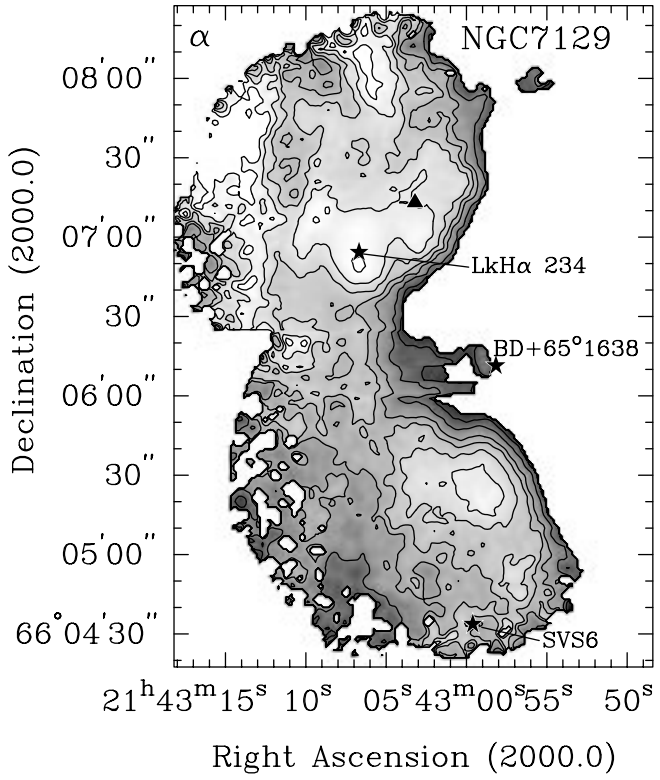

FIG. 6.—Spectral index α map ($F_\nu \sim \nu^\alpha$) obtained from the (14″ beam size) 850 and 450 μm maps. Gray-scale contours range from 3 to 5, with a step of 0.25, where dark color implies high spectral index. The optical positions are marked with stars and the LkHα234 SMM 2 source with a triangle.

presented by Fuente et al. (1998) as a dense gas condensation. Two of our $C^{18}O$ $J = 3$–2 spectra, at offsets 3 and 6 in Table 2, are close to SMM 2, i.e., $\sim 5''$ north and south of the submillimeter peak. They show slightly elevated excitation temperatures (see Table 2), but the higher kinetic temperature is more likely due to the PDR rim than to any embedded source. The line widths, especially in $C^{18}O$, are narrow, and there is no evidence for outflow. SMM 2 therefore has the appearance of a prestellar core. The virial mass is $\sim 8.2\ M_\odot$, assuming a line width of 1 km s^{-1} and a diameter of $\sim 14''$, i.e., several times larger than the mass we derive from our submillimeter observations. However, it is clear that the hot gas in the cavity has compressed the whole ridge in which SMM 2 is embedded. We also note that our derived value for β as well as our assumed dust temperature is rather uncertain and our mass estimate is at most accurate to a factor of 2. SMM 2 could therefore either be a prestellar core or a protostar.

4.3. *Dust Properties*

To investigate dust properties across the region, a map of the spectral index α ($F_\nu \sim \nu^\alpha$) was made, using the 850 and 450 μm deconvolved images smoothed to 14″ resolution. Explicitly,

$$\alpha = \frac{\log\,(F_{\lambda_1}/F_{\lambda_2})}{\log\,(\lambda_2/\lambda_1)}\,, \tag{4}$$

where λ_1 and λ_2 are the two wavelengths used in our observations.

We know that the maps are distorted by chopping into the cloud emission (§ 3.2). This will affect the 450 μm more than the 850 μm flux, because the error lobe is larger at 450 μm. The 450 μm map was therefore corrected by adding a constant level of 5% of the peak value to the map, before convolving it to a resolution of 14″. The resulting map is shown in Figure 6.

The spectral index map has two trends. First, a comparison with the 450 or 850 μm map shows a general anticorrelation between submillimeter continuum flux and spectral index. The highest flux positions are minima of α, and the value of α increases toward regions of weaker continuum emission. The α minima are seen at locations correlating with dense gas clumps, LkHα 234 SMM 1, SMM 2, and the flux peak near the offset ($-45\farcs0, -85\farcs0$). The curving ridge of 450 μm emission (Fig. 4) can be followed throughout its length in the α map. Second, the map also shows a steep rise in α toward the molecular cavity. This large gradient in α occurs along the entire transition region.

It is important to determine whether the observed increase in α is due to the change in temperature through the PDR, or in the dust opacity index, β. Because $F_\nu \propto \kappa_\nu^\beta B_\nu (T_d)$, the spectral index, α, and the dust opacity, β, can be related as follows:

$$\alpha = \beta + 2 + \gamma , \tag{5}$$

where γ can be thought of as a correction to the Rayleigh-Jeans form of the Planck function and is given by (Visser et al. 1998)

$$\gamma = 1 - \frac{\log \left[(e^{h\nu_{850}/kT} - 1)/(e^{h\nu_{450}/kT} - 1)\right]}{\log (\nu_{850}/\nu_{450})} . \tag{6}$$

An increase in α may be due to an increase in the dust temperature, T, and/or in β. The temperature is expected to be higher in the cavity because of the more intense radiation field. Our analysis in § 3.1 showed that the gas temperature is higher toward the ridge. Is it possible to understand the larger values of α only as due to higher dust temperatures? The answer is no because γ approaches zero at large T so that the maximum value of α is $\beta + 2$. Values of α larger than 4 require $\beta \geq 2$, even if T is large. While the expected increase in T_d toward the cavity will result in higher values of α, the increase in T_d must be accompanied by an increase in β.

Ideally, the above relations can yield the exact value of β if one knows the spectral index α and the temperature of the dust. In practice, the determination of the true value of β is restricted by the current uncertainties in the submillimeter fluxes, especially at short wavelengths, which will reflect into uncertainties in α. The dust will be more optically thick at 450 μm than at 850 μm (since the optical depth changes with frequency as $\tau \propto \nu^\beta$). Thus, at 450 μm we do not see as deeply into the densest hot cores as one does at 850 μm. Another more severe restriction is our ability to accurately measure the submillimeter fluxes, especially at short wavelengths. As mentioned before, we tried to remedy this situation by adding a constant zero level to the 450 μm flux, but this is only a first-order correction. In reality, the dust structure will not be flat but will have its own substructure, similar to that of the molecular cloud. Therefore, the numerical values of α in regions of low flux are highly uncertain.

In summary, we have confidence in the values of $\alpha \simeq 3$ that we find at high-flux levels. We also believe in the trend of increasing α toward lower flux values. In the dense cores we find $\beta < 2$, as suggested by the minima in the spectral index plot as well as our dust fits in Figure 5. Since small grains produce a high-β index and large grains lead to smaller values of β, our results are consistent with the growth of grains in regions of high density.

These present observations of NGC 7129 support the conclusions of other similar studies that high-density clumps or cores have smaller values of β than does the surrounding gas (Visser et al. 1998; Johnstone & Bally 1999; Sandell et al. 1999). Values of $\beta \sim 2$ outside the flux peaks have been also reported in reflection nebulae surrounding Herbig Ae/Be stars (Whitcomb et al. 1981). Our α map goes further, however, in showing a general correspondence between flux and α over an extended area, and in showing a steep increase in α (and, therefore, in β) along an extended PDR.

5. SUMMARY

New high-resolution maps of the NGC 7129 ridge have been obtained, both in submillimeter continuum emission and in ^{13}CO $J = 3$–2 line emission. The main results of this study are the following:

1. A sharp boundary between the molecular ridge and cavity is clearly seen in the ^{13}CO map. A previously detected narrow filament of optical and near-infrared emission follows closely the cloud-cavity boundary. Strong emission in the $v = 1$–0 $S(1)$ line of H_2 from the filament, if due to fluorescence, supports the interpretation of the boundary as a PDR.

2. The ^{13}CO emission consists of two main cloud cores connected by a bridge of gas. The northern cloud core has three ^{13}CO peaks, while the southern one has a single extended peak.

3. The 850 and 450 μm maps show a very good morphological agreement with the ^{13}CO map. Both data sets show a sharp boundary (cloud rim) toward the cavity where the two young stars BD +65°1637 and BD +65°1638 are located.

4. Three compact sources are seen in the continuum maps (SMM 1, SMM 2, and FIRS 2 in Table 3). Isothermal graybody fits to the measured spectral energy distributions have been made by combining our SCUBA data with earlier observations. The resulting masses, dust temperatures, luminosities, and dust emissivities are given in Table 4. The SMM 1 continuum peak is identified with the deeply embedded infrared source IRS 6, which according to these present fits is a young Herbig Be star.

5. For nine offsets around the LkHα 234 star, the ^{13}CO/C^{18}O intensity ratio was used to obtain the mass of gas in an 14″ beam. The masses derived from CO are found to be consistent with masses derived from the dust continuum emission. Within our analysis uncertainties, the results are consistent with little or no CO depletion in this region.

6. A map of the 850 μm/450 μm spectral index, α, shows a general correlation between the α minima and the submillimeter continuum flux peaks. The low values of α in the peaks also correlate with low values of dust opacity indices, β, in the range 1–1.6, derived for the compact source, suggesting grain growth. The spectral index α rises steeply toward the molecular cavity, along the entire length of the boundary region. Consequently, the dust opacity index in this region is also high, $\beta \sim 2$. This suggests very hot, small

size grains in the PDR ridge, whose mantles have been evaporated by the intense UV radiation.

We would like to thank the anonymous referee for the valuable comments that helped improve our paper. The James Clerk Maxwell Telescope is operated on a joint basis between the United Kingdom Particle Physics and Astronomy Research Council (PPARC), the Netherlands Organization for the Advancement of Pure Research (ZWO), the Canadian National Research Council (NRC), and the University of Hawaii (UH). This research was partly supported by an operating grant from the Natural Sciences and Engineering Research Council of Canada.

REFERENCES

Ábrahám, P., Balázs, L. G., & Kun, M. 2000, A&A, 354, 645
Bechis, K. P., Harvey, P. M., Campbell, M. F., & Hoffmann, W. F. 1978, ApJ, 226, 439
Bertoldi, F., & Draine, B. T. 1996, ApJ, 458, 222
Bertout, C. 1987, in IAU Symp. 122, Circumstellar Matter, ed. I. Appenzeller & C. Jordan (Dordrecht: Reidel), 23
Bertout, C., & Thum, C. 1982, A&A, 107, 368
Cabrit, S., Lagage, P. O., McCaughrean, M., & Olofsson, G. 1997, A&A, 321, 523
Cesarsky, C. J., Cesarsky, D. A., Churchwell, E., & Lequeux, J. 1978, A&A, 68, 33
Clements, E. D., & Argyle, R. W. 1984, MNRAS, 209, 1
Dent, W. R. F., Sandell, G., Duncan W. D., & Robson, E. I. 1989, MNRAS, 238, 1497
Di Francesco, Evans, N. J., II, & Harvey, P. M. 1998, ApJ, 509, 324
Edwards, S., & Snell, R. L. 1983, ApJ, 270, 605
Eiróa, C., Palacios, J., & Casali, M. M. 1998, A&A, 335, 243
Frerking, M. A., Langer, W. D., & Wilson, R. W. 1982, ApJ, 262, 590
Fuente, A., Martín-Pintado, J., Bachiller, R., Neri, R., & Palla, F. 1998, A&A, 334, 253
Giannini, T., et al. 1999, A&A, 346, 617
Goodrich, R. W. 1986, AJ, 92, 885
Güsten, R., & Marcaide, J. M. 1986, A&A, 164, 342
Hartigan, P., & Lada, C. 1985, ApJS, 59, 383
Harvey, P. M., Wilking, B. A., & Joy, M. 1984, ApJ, 278, 156
Henning, Th., Burkert, A., Launhardt, R., Leinert, C., & Stecklum, B. 1998, A&A, 336, 565
Herbig, G. H., & Bell, K. R. 1988, Lick Obs. Bull., 1111
Hildebrand, R. H. 1983, QJRAS, 24, 267
Hodapp, K. W. 1994, ApJS, 94, 615
Holland, W. S., et al. 1999, MNRAS, 303, 659
Hollenbach, D. J., & Tielens, A. G. G. M. 1997, ARA&A, 35, 179
Jenness, T., & Lightfoot, J. F. 1999, Starlink User Note 216.6, Rutherford Appleton Lab., PPARC
Jenness, T., Scott, P. F., & Padman, R. 1995, MNRAS, 276, 1024
Johnstone, D., & Bally, J. 1999, ApJ, 510, L49
Lorenzetti, D., et al. 1999, A&A, 346, 604
Miranda, L. F., Eiróa, C., Fernández, M., & Gomez de Castro, A. I. 1994, A&A, 281, 864
Mitchell, G. F., & Matthews, H. E. 1994, ApJ, 423, L55
Padman, R. 1992, SPECX V6.3 User's Manual (Cambridge: Cavendish Lab.)
Racine, R. 1968, AJ, 73, 233
Ray, T. P., Poetzel, R., Solf, J., & Mundt, R. 1990, ApJ, 357, L45
Rodríguez, L. F., Moran, J. M., Ho, P. T. P., & Gottlieb, E. W. 1980, ApJ, 235, 845
Sandell, G. 1997, Starlink Cookbook 11.1, Rutherford Appleton Lab., PPARC
———. 2000, A&A, 358, 242
Sandell, G., et al. 1999, ApJ, 519, 236
Sandell, G., & Olofsson, H. 1981, A&A, 99, 80
Sandell, G., & Weintraub, D. 1994, in ASP Conf. Ser. 62, The Nature and Evolutionary Status of Herbig Ae/Be Stars, ed. P. S. Thé, M. R. Pérez, & E. P. J. van den Heuvel (San Francisco: ASP), 261
Sault, R. J., Teuben, P. J., & Wright, M. C. H. 1995, in ASP Conf. Ser. 77, Astronomical Data Analysis Software and Systems IV, ed. R. A. Shaw, H. E. Payne, & J. J. E. Hayes (San Francisco: ASP), 433
Shevchenko, V. S., & Yabukov, S. D. 1989, Soviet Astron., 33, 370
Skinner, S. L., Brown, A., & Steward, R. T. 1993, ApJS, 87, 217
Visser, A. E., Richer, J. S., Chandler C. J., & Padman, R. 1998, MNRAS, 301, 585
Weintraub, D. A., Kastner, J. H., & Mahesh, A. 1994, ApJ, 420, L87
Whitcomb, S. E., Gatley, I., Hildebrand, R. H., Keene, J., Sellgren, K., & Werner, M. W. 1981, ApJ, 246, 416
Wilking, B. A., Mundy, L. G., & Schwartz, R. D. 1986, ApJ, 303, L61
Wilson, T. L., & Rood, R. T. 1994, ARA&A, 32, 191

Note added in proof.—During the time since this paper has been reviewed, we learned that a similar study on the NGC 7129 region has been reported by A. Fuente et al. (2001, A&A, 366, 873).